Electron–hole separation in ferroelectric oxides for efficient photovoltaic responses

Donghoon Kim[a], Hyeon Han[b], June Ho Lee[b], Jin Woo Choi[c], Jeffrey C. Grossman[d], Hyun Myung Jang[a,b,1], and Donghun Kim[e,1]

[a]Division of Advanced Materials Science, Pohang University of Science and Technology, 37673 Pohang, Republic of Korea; [b]Department of Materials Science and Engineering, Pohang University of Science and Technology, 37673 Pohang, Republic of Korea; [c]Advanced Photonics Research Institute, Gwangju Institute of Science and Technology, 61005 Gwangju, Republic of Korea; [d]Department of Materials Science and Engineering, Massachusetts Institute of Technology, Cambridge, MA 02139; and [e]Computational Science Research Center, Korea Institute of Science and Technology, 02792 Seoul, Republic of Korea

Edited by Thomas E. Mallouk, The Pennsylvania State University, University Park, PA, and approved May 18, 2018 (received for review December 13, 2017)

Despite their potential to exceed the theoretical Shockley–Queisser limit, ferroelectric photovoltaics (FPVs) have performed inefficiently due to their extremely low photocurrents. Incorporating Bi_2FeCrO_6 (BFCO) as the light absorber in FPVs has recently led to impressively high and record photocurrents [Nechache R, et al. (2015) *Nat Photonics* 9:61–67], which has revived the FPV field. However, our understanding of this remarkable phenomenon is far from satisfactory. Here, we use first-principles calculations to determine that such excellent performance mainly lies in the efficient separation of electron–hole (*e-h*) pairs. We show that photoexcited electrons and holes in BFCO are spatially separated on the Fe and Cr sites, respectively. This separation is much more pronounced in disordered BFCO phases, which adequately explains the observed exceptional PV responses. We further establish a design strategy to discover next-generation FPV materials. By exploring 44 additional Bi-based double-perovskite oxides, we suggest five active-layer materials that offer a combination of strong *e-h* separations and visible-light absorptions for FPV applications. Our work indicates that charge separation is the most important issue to be addressed for FPVs to compete with conventional devices.

ferroelectrics | double perovskites | photovoltaics | *e-h* separation | density functional theory

Ferroelectrics have long garnered attention in light-to-electricity conversion devices owing to their anomalously high photovoltages (1–7), coupled with their reversibly switchable photocurrents (8, 9). However, ferroelectric photovoltaics (FPVs) suffer from extremely low photocurrents (on the order of microamperes per square centimeter under 1 sun illumination), which has mainly been attributed to the wide band gap energy (>2.5 eV) of the active-layer materials [e.g., $BiFeO_3$ (BFO) and $Pb(Zr_xTi_{1-x})O_3$ (PZT)] (10, 11). Tremendous efforts have been made to overcome this challenge, utilizing techniques such as band gap tuning (5, 12–14), domain structure manipulation (2, 15), and multijunction stacking (16, 17). Unfortunately, the power conversion efficiencies (PCEs) of FPVs have, until recently, remained too low ($\ll$1%) to be utilized in practical PV applications (6).

In this regard, the recent work of Nechache et al. (18) is highly noteworthy, in which a new light-absorbing material, namely, Bi_2FeCrO_6 (BFCO) in a double-perovskite structure, was employed. In 2005, Baettig et al. (19, 20) predicted from first-principles calculations that multiferroic BFCO simultaneously possesses large spontaneous polarization and magnetization above room temperature. Motivated by this ab initio prediction, Nechache et al. (21–23) synthesized BFCO-based multilayers using the pulsed laser deposition technique. Incorporating BFCO as the light absorber remarkably improved the FPV device performance: Photocurrents on the order of tens of milliamperes per square centimeter and a record PCE of 8.1% were achieved (18). This work is indeed a breakthrough, as it solved the biggest problem (i.e., low photocurrent) that FPVs have faced since their inception.

Herein, we reveal the main origin of the phenomenal performance of BFCO-based FPVs to be efficient electron–hole (*e-h*) separations. Utilizing ab initio density functional theory (DFT) calculations, we show that the photoexcited *e-h* pairs in BFCO are spatially separated on Fe and Cr sites, respectively, irrespective of the configuration (spatial arrangement) of the B-site cations, leading to low charge recombination rates. This is in sharp contrast to the parent BFO material, in which both electrons and holes occupy the same Bi sites, which increases the *e-h* recombination rate. We further find that the positional disordering of B-site cations in BFCO substantially enhances the degree of *e-h* separation, which is critical to understanding the observed exceptional PV responses. With this knowledge, we then establish a design strategy to search for next-generation FPV materials that can potentially outperform BFCO. We explore 44 additional Bi-based ferroelectric oxides in a double-perovskite structure and suggest five materials that offer the combined benefits of efficient *e-h* separations and visible-light absorptions for FPV applications.

Results and Discussion

The observed remarkable performance of BFCO-based FPVs, compared with that of prototypical BFO-based FPVs, was previously thought to benefit mainly from the band gap reduction and the resultant increase in solar absorption (18). Although it is true

Significance

Photovoltaics (PVs) benefitting from ferroelectric polarizations can overcome critical limitations of conventional type PVs. In this class, Bi_2FeCrO_6 is known to be the best-performing material; however, a fundamental understanding of the origin is lacking, which has limited further performance improvements. Here, we carried out a theoretical investigation of the electronic structure of this material. As a result, electron–hole (*e-h*) pairs are observed to separate upon photoexcitation, which can be a dominant underlying mechanism for the exceptional PV responses. Based on this understanding, we further suggest five novel materials that can offer a combination of strong *e-h* separations and visible-light absorptions. We expect the community of ferroelectric PVs to immediately benefit from the features of the new suggested materials.

Author contributions: H.M.J. and Donghun Kim designed research; Donghoon Kim and Donghun Kim performed research; Donghoon Kim, H.H., J.H.L., and Donghun Kim analyzed data; Donghoon Kim, J.C.G., H.M.J., and Donghun Kim wrote the paper; and J.W.C. provided constructive comments on revision.

The authors declare no conflict of interest.

This article is a PNAS Direct Submission.

[1]To whom correspondence may be addressed. Email: hmjang@postech.ac.kr or donghun@kist.re.kr.

This article contains supporting information online at www.pnas.org/lookup/suppl/doi:10.1073/pnas.1721503115/-/DCSupplemental.

Published online June 11, 2018.

that the enhanced solar absorption is an important factor, the magnitude of its contribution has not been quantified. Here, we clarify this point by experimentally measuring the PV parameters of BFO-based cells and comparing these with literature values of BFCO-based cells under the same device architectures [i.e., active-layer thickness (100 nm), substrate ($SrTiO_3$), electrodes (ITO, $SrRuO_3$)]. Under AM1.5G illumination, the short-circuit current (J_{sc}) of the reference thin-film BFO cell is ~11.6 μA·cm^{-2}, while the J_{sc} of the BFCO-based cell is 11.7 mA·cm^{-2}. Note the three-orders-of-magnitude difference in the J_{sc} values (see *SI Appendix*, Fig. S1 and Tables S1 and S2 for detailed comparisons). Next, we compare the solar absorption (A) of the BFO and BFCO films using Eq. **1**,

$$A(\%) = \left(1 - \frac{\int_0^{E_g} S_E dE}{\int_0^{\infty} S_E dE} - \frac{\int_{E_g}^{\infty} \exp(-\alpha d) S_E dE}{\int_0^{\infty} S_E dE}\right) \times 100, \qquad [1]$$

where S_E is the solar irradiance as a function of photon energy E, α is the E-dependent absorption coefficient, and d is the film thickness. As shown in Fig. 1*A*, the BFCO film exhibits a relatively lower absorption onset energy, enabling the absorption of sunlight in the visible range. As a result, the BFCO layer can absorb ~4.5 times more sunlight than the BFO layer at the same film thickness of 100 nm (Fig. 1*B*). These comparisons indicate that the increased solar absorption in the BFCO film (only a 4.5-fold enhancement) cannot be the primary factor responsible for the three-orders-of-magnitude change in the J_{sc}. Thus, the main cause of the remarkably enhanced J_{sc} in BFCO is now an open question.

To reveal the origin of this exceptional PV response, we investigated the electronic structure of BFCO. Modeling BFCO requires a large set of computations due to the complexity of the atomic and magnetic orderings. Fig. 1*C* shows the BFCO model structures used in our simulations. Because the 3D configuration of the B-site cations (i.e., Fe and Cr) in BFCO varies significantly with deposition conditions (18), we considered 10 possible B-site cation configurations in 40-atom unit cells (eight formula units) while maintaining the Fe:Cr ratio at 1:1. These include nine disordered structures (labeled d_1 to d_9) and the remaining ordered structure in which the Fe and Cr planes alternate along the [111] direction. In addition to the atomic configurations, magnetic orderings were also considered in the present work (Fig. 1*D*, *Inset*), as these orderings can be varied through thermal excitation (24) or pressure-induced transitions (25). As BFCO is known to have antiferromagnetic (AFM) ordering, we considered three different types of AFM orderings, namely, A, C, and G types, for each atomic configuration.

In Fig. 1*D*, the computed band gap (E_g) is plotted as a function of the corresponding Kohn–Sham (K-S) energy for all samples of investigation in this work. For ordered BFCO, both K-S energy and E_g are little dependent on the spin states: the A, C, and G AFM orderings are nearly degenerate in K-S energy, and also are similar (1.43 eV to 1.65 eV) in E_g. Unlike the ordered case, due to the complexity of atomic configurations, a total of 27 disordered samples [9 (atomic) × 3 (spin)] can possibly occur, and their energies vary across a wide spectrum. Therefore, it is important to sample those that can most likely occur in experiments by comparing their K-S energies and E_g values. It is well known that disordered BFCO phases are more stable and also exhibit larger E_g (up to 2.4 eV) than ordered ones (18). We found that disordered samples of C AFM or G AFM possess lower K-S energies and larger E_g values compared with ordered ones, whereas the opposite was observed for A AFM. Thus, our analysis confirms that C and G AFM orderings well represent the spin states in the disordered BFCO phases observed in experiments (18) while A AFM ordering is highly unlikely to appear (*SI Appendix*, Table S3).

As our model captured the key characteristics of BFCO, we went on to calculate the electronic structures of BFCO and compared them with the tetragonal BFO system. For detailed analysis, we focus only on three selected cases: (*i*) BFO structure in C AFM (*ii*), ordered BFCO in C AFM, and (*iii*) "d_1" structure in C AFM (as a representative of disordered BFCO). Fig. 2 *A*–*C* illustrates the orbital-resolved band structures and the corresponding density of states (DOS) of these three selected cases. For the tetragonal BFO (Fig. 2*A*), the edge of the highest valence band (VB) at the Γ-point is predominantly contributed by Bi 6*s*–O 2*p* hybrid states, and the lowest conduction band (CB) at the same Γ-point mainly consists of Bi 6*p* states. Importantly, note that, unlike rhombohedral BFO (26) in which the CB edge largely consists of Fe 3d states, Bi orbitals mainly contribute to the edges of both the VB and CB states (27) in tetragonal BFO. In contrast, the orbital constitutions near band edges in BFCO (Fig. 2 *B* and *C*) completely differ from

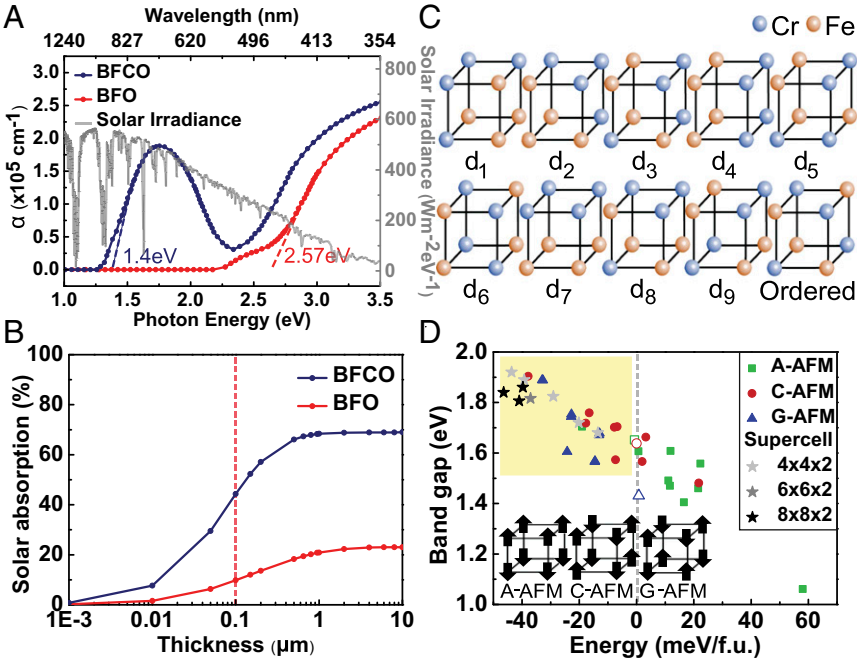

Fig. 1. Solar absorption, ion configurations, and band gaps of BFCO materials. (*A*) Absorption coefficient α [reproduced from $(\alpha E)^2$ vs. E plots provided in ref. 18] plotted as a function of the photon energy. The gray line represents the AM1.5G (100 mW/cm^2) solar irradiance. (*B*) Thickness-dependent solar absorption (percent) curves of the BFO and BFCO films. (*C*) Schematic diagrams of 10 possible B-site cation configurations in 40-atom BFCO unit cells, including the ordered case. The nine disordered structures are labeled from d_1 to d_9. (*D*) Band gap vs. K-S energy plot for all BFCO samples investigated in this work. Ordered structures are shown by open symbols (near energy = 0 eV). Larger supercells of $n = 4$, 6, 8 are shown by gray stars. The energy in the abscissa is referenced to the K-S energy of the ordered BFCO in C AFM. Samples in the yellow-shaded region well represent the disordered BFCO phases observed in experiments. The *Inset* represents the spin ordering of A, C, and G AFM.

those in BFO. For both ordered and disordered BFCO case, broad Cr 3*d* (t_{2g})–O 2*p* hybrid states dominate the top of the VB (at the A point in Fig. 2*B* and at the M point in Fig. 2*C*), and relatively narrower Fe 3*d* (t_{2g}) states form the bottom of the CB (at the Z point in Fig. 2*B* and at the M point in Fig. 2*C*). For a visual confirmation, the computed charge densities of the CB minimum (CBM) and VB maximum (VBM) states of the three different cases are shown in Fig. 2 *D*–*F*. For BFO (Fig. 2*D*), both the electron and hole density are located at the Bi sites. In contrast, both the ordered and disordered BFCO (Fig. 2 *E* and *F*) show a distinct spatial separation of the electron and hole densities into Fe and Cr sites, respectively, which would result in much easier separations of the photoexcited *e*-*h* pairs in BFCO. Although only selected cases are shown in the main text, the band structures and DOS of all other atomic and magnetic configurations were found to be qualitatively very similar (*SI Appendix*, Figs. S2 and S3).

We then examined the enhanced *e*-*h* recombination lifetime (τ) in BFCO over that of the reference BFO system. Based on Fermi's golden rule, the *e*-*h* recombination rate ($1/\tau$) can be written as (28)

$$\frac{1}{\tau}=\frac{4\ \alpha\omega n}{3\ m^2c^2}[\langle e|\ p|h\rangle]^2, \qquad [2]$$

where ω is the photon frequency, n is the refractive index, α is the fine-structure constant, and $\langle e|p|h\rangle$ is the momentum matrix element between the electron and hole states. Under the Schrödinger picture based on the electric dipole approximation (29), the momentum matrix element becomes $+im\omega\langle e|r|h\rangle$. In tetragonal BFO, the VBM mostly consists of the Bi 6*s* orbital (even parity) at the Bi ion site, while the CBM mostly consists of the 6*p* orbital (odd parity) at the same Bi ion site. Thus, the effective matrix element of the VBM–CBM interband transition, $\langle e|r|h\rangle$, becomes an even-parity function, the integration of which will survive as a nonzero value. In contrast, in BFCO, the matrix element vanishes to zero since the Fe (CBM) and Cr (VBM) ion sites are spatially separated by an oxygen ion, i.e., Fe–O–Cr. Even if the two ions were intimately (hypothetically) close to one another, a symmetry argument would further prohibit a

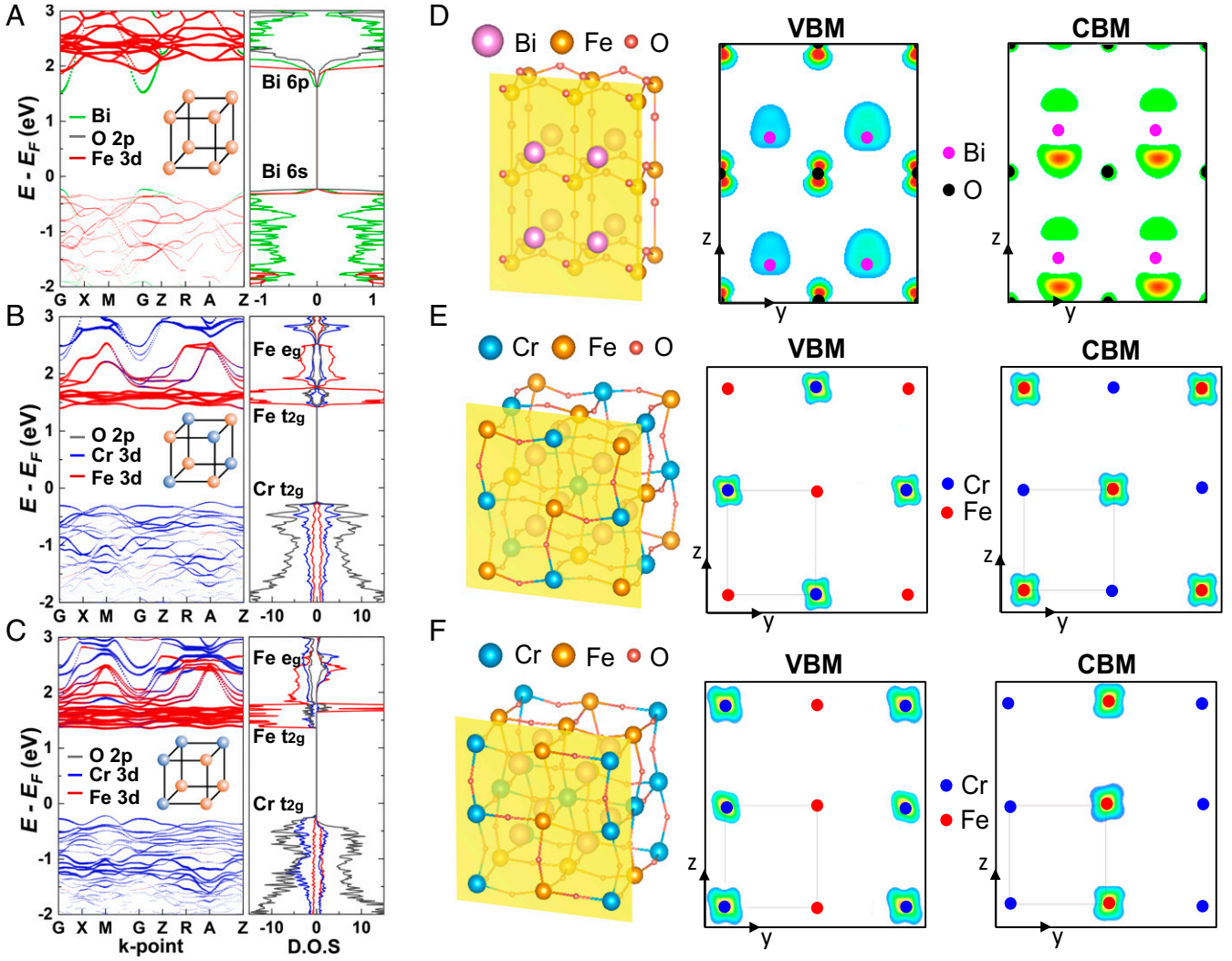

Fig. 2. Electronic structures of BFO and BFCO. (*A*–*C*) Calculated orbital-resolved band structures and the corresponding DOS of (*A*) BFO in C AFM, (*B*) ordered BFCO in C AFM, and (*C*) "d_1" structure (disordered) BFCO in C AFM. In the band structure plots, the red, blue, and green colors indicate the contributions of the Fe 3*d*, Cr 3*d*, and Bi orbitals, respectively. Similarly, in the DOS plots, the red, blue, green, and gray lines represent the Fe 3*d*, Cr 3*d*, Bi, and O 2*p* states, respectively. (*D*–*F*) The 2 × 2 × 2 supercell structures (*Left*), and 2D cross-sections of the partial charge densities of the VBM (*Middle*) and CBM (*Right*) states: (*D*) BFO in C AFM, (*E*) ordered BFCO in C AFM, and (*F*) "d_1" disordered BFCO in C AFM. Note that, in *E* and *F*, oxygen atoms and their contributions are not shown for clarity, as they are out of the cross-section planes. The 3D plots of the partial charge densities are available in *SI Appendix*, Fig. S4.

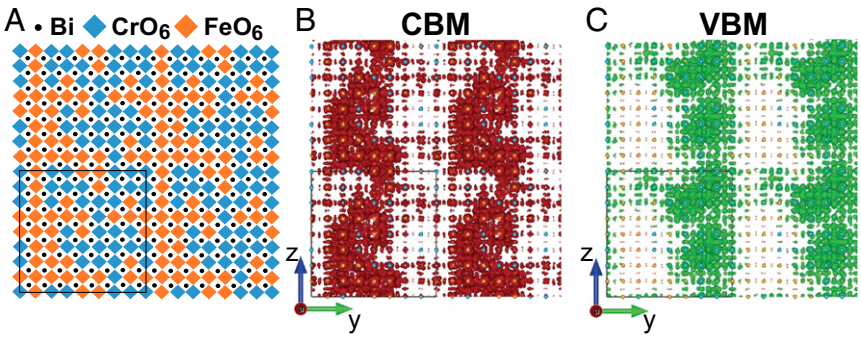

Fig. 3. Distinct *e-h* separation in disordered BFCO on a large scale. (*A*) Schematic of the tested 8 × 8 × 2 supercell. (*B* and *C*) Partial charge densities of the (*B*) CBM (in the red cloud) and (*C*) VBM (in the green cloud) states. CBM and VBM states are spatially separated onto the Fe-rich vs. Cr-rich domains, respectively.

nonzero matrix element since $\langle e|\mathrm{r}|h\rangle = \langle \psi_{CBM}|\mathrm{r}|\psi_{VBM} = \psi_{t_{2g}(Fe)}|\mathrm{r}|\psi_{t_{2g}(Cr)}\rangle = \int \text{even} \otimes \text{odd} \otimes \text{even}\, dv = 0$. Then, Eq. **2** predicts that the lifetime ratio asymptotically approaches infinity, namely, $\tau_{BFCO}/\tau_{BFO} \to \infty$. Thus, this comparison clearly shows that double-perovskite BFCO would have a much longer *e-h* recombination lifetime than single-perovskite BFO.

On the other hand, the small transition moment integral indicates that the probability of the across-band gap excitation will also be very small, which may seemingly contradict the fact that BFCO absorbs visible lights strongly (18). Comparing the experimental absorption spectra and our own optical calculations (*SI Appendix*, Fig. S5), we observe that the strong absorption is enabled by the absorption of light about 0.4 eV to 0.45 eV above the electronic band gap, even though the gap transition is severely limited. Such behavior is due to the peculiar electronic structure of BFCO where Cr e_g states contribute a fair amount at higher energy states (i.e., CBM of +0.4 eV and above), leading to the strong Cr t_{2g}-to-Cr e_g transitions (*SI Appendix*, Fig. S6). Therefore, while the VBM-to-CBM excitations (Cr t_{2g}-to-Fe t_{2g}) are limited, the Cr t_{2g}-to-Cr e_g transition can strongly occur at the photon energy about 0.4 eV higher than E_g. The photoexcited electrons will then rapidly relax to the CBM state where Fe t_{2g} dominates; hence the *e-h* recombination lifetime will be greatly extended due to a very small transition moment integral of the gap transition (i.e., $\langle e|p|h\rangle \approx 0$).

To describe more realistic and disordered BFCOs, it is necessary to investigate the charge separation phenomenon in much larger scales. The disordered samples (d_1 to d_9) in Fig. 1*C* are, in fact, not fully disordered, due to their small cell sizes. To resolve this critical issue, we built much larger supercells of $n \times n \times 2$ ($n = 4, 6, 8$) containing up to 640 atoms per cell. Unfortunately, for such large cells, exploring all possible spin (magnetic) configurations is not practically feasible. Thus, the magnetic configurations should be properly chosen to guarantee that our supercells reproduce the real charge distribution. Based on the Goodenough–Kanamori rule (30, 31) and our spin-coupling energy model (*SI Appendix*, Table S3), the spin states of the B-site ions can be carefully deduced obeying the following rule: Nearest-neighbor (NN) Fe–Fe or Cr–Cr pairs tend to have antiparallel (↑↓) spins. We observe that all large supercells obeying this rule possess lower K-S energies and larger band gaps than ordered BFCO, as shown in Fig. 1*D*; thus, they well represent more realistic and disordered BFCOs observed in experiments.

The electron and hole densities of a select disordered BFCO simulated in the largest supercell (8 × 8 × 2 cell) are shown in Fig. 3. Comparing charge density distributions in Fig. 3 *B* and *C*, we found that CBM and VBM states are clearly separated into Fe-rich and Cr-rich domains, and the degree of separation is much more pronounced than in the small-cell cases. This result is attributed to the formation of BFO-like and $BiCrO_3$-like domains (Fig. 3*A*), and the generation of long-range connectivity of each domain in disordered BFCO samples (*SI Appendix*, Fig. S7). Such distinct separation phenomenon is found to be very general, irrespective of the supercell size or B-site ion configuration (*SI Appendix*, Fig. S8); thus, the disordering of B-site ions substantially enhances the *e-h* separation. This finding can adequately explain a prior experimental observation that FPVs utilizing fully ordered BFCO perform much less efficiently (18), and confirms the importance of disordered BFCO phases for efficient PV responses. These results indicate that the efficient charge separation can be a dominant underlying mechanism for the exceptional PV responses in BFCO-based PV cells.

The disordering of B-site cations not only enhances *e-h* separation but also greatly influences the charge transport properties in BFCO. Using DFT, we calculated the charge transport properties, namely, the effective masses of the photoexcited electron and hole. In Fig. 4, the effective masses of the ordered and disordered structures (d_1 to d_9) are compared. Note that A AFM ordering was not considered, due to its relative instability (Fig. 1*D*). A prominent feature observed in Fig. 4 is that B-site ion disordering significantly reduces the effective mass of the electron (m_e^*). The mass of ordered BFCO is extremely large (47.3 m_0 for C AFM and 44.3 m_0 for G AFM). However, for most of the disordered BFCO cases (16 out of total 18 test samples), the electron becomes much lighter, showing an effective mass between 1.1 m_0 and 10.3 m_0. Only two cases (d_3 and d_6 in G AFM) deviate from the general trend, and exhibit large m_e^* values (43.9 m_0 and 34.8 m_0, respectively) comparable to that of ordered BFCO. In real BFCO films, all of these 18 disordered

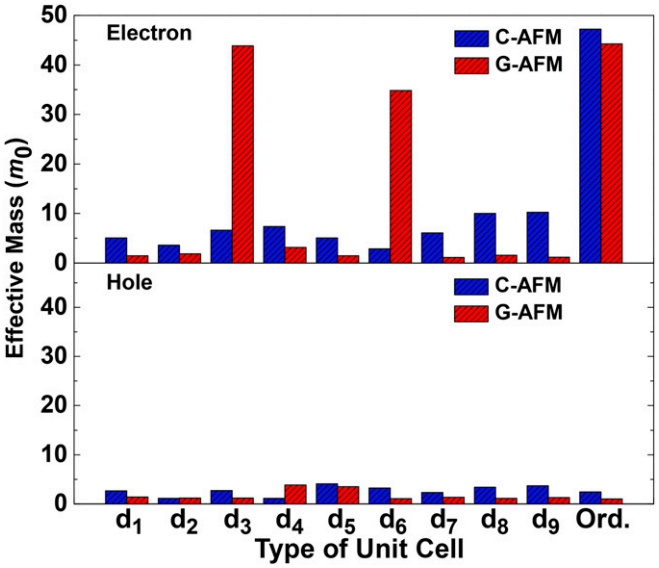

Fig. 4. B-site ion configuration-dependent charge transport properties. Calculated electron (*Upper*) and hole (*Lower*) effective masses in the direction of polarization (i.e., *z* axis) for ordered BFCO and disordered BFCO (d_1 to d_9).

structures are likely to exist, owing to their low and similar energies; thus, electrons would be, on average, much more mobile in the disordered domains (averaged mass of 8.2 m_0) than in the ordered domains (averaged mass of 45.8 m_0). In contrast, the impact of B-site ion disordering on the effective mass of the hole (m_h*) is small. The effective masses of the holes are found to be quite small, in the range between 1.0 m_0 and 4.0 m_0, for both ordered and disordered geometries. See *SI Appendix*, Fig. S9 and Table S4 for detailed orbital analysis, which explains the different quantities and behaviors of the electron and hole masses.

With the knowledge accumulated from the study of BFCO, we provide a design strategy to search for next-generation FPV materials. We explored 44 additional oxides based on the following three criteria: (*i*) efficient *e-h* separation, (*ii*) low K-S band gap, and (*iii*) strong visible-light absorption (Fig. 5*A*), with the aim of discovering light-absorbing materials in FPVs. The tested materials are all Bi-based double-perovskite structured oxides, i.e., $Bi_2(B',B'')O_6$ where (B′,B″) is any possible combination of transition-metal B-site cations. For each (B′,B″) combination, six thermodynamic phases were investigated: $Fm\bar{3}m$, R3, $P4/mnc$, $I4/m$, $P2_1/n$, and $I2/m$ (32). The energies of all six phases were compared, and only the most stable phase was considered in the subsequent screening process. The first criterion is the degree of *e-h* separation, R (defined in *Methods*). The material with a negative R value offers efficient spatial charge separation onto B′ and B″ cation sites (Fig. 5*B*). Out of 45 test sets (including BFCO), 10 (B′,B″) combinations showed negative R values, shown, as follows, in the order of strong to weak separation: (Ti,V), (V,Cu), (Ti,Mn), (V,Mn), (Ti,Fe), (Cr,Ti), (Fe,Cr), (Co,Cr), (Mn,Co), and (Fe,V). Note that, for these 10 (B′,B″) systems, the CBM and VBM states are spatially separated onto B′ and B″ sites, respectively. Inspiringly, six of these suggested materials show even stronger *e-h* separations than BFCO.

The second criterion is a low enough band gap (E_g < 2.0eV). Out of 10 aforementioned materials, only (Ti,Mn) failed to satisfy this requirement, leaving nine materials in the candidate pool. It is, however, important to remember that strong absorptions likely occur at photon energy much larger than an electronic gap of R < 0 in these materials, which necessitates the additional optical calculations to see if visible light absorptions are actually feasible. In this regard, the third criterion is a low enough optical threshold energy, i.e., E_{opt} < 2.0eV (E_{opt} defined in *Methods*). Out of nine remaining materials, three materials of [(V,Mn); E_{opt} = 2.27 eV], [(Ti,Fe); E_{opt} = 2.74 eV], and [(Cr,Ti); E_{opt} = 2.7 eV] failed to stay in the top candidate list, due to the particularly large difference (>1.0 eV) between E_g and E_{opt} (*SI Appendix*, Fig. S10). As a result, the remaining five materials of [(Ti,V); R = −0.89, E_{opt} = 1.46 eV], [(V,Cu); R = −0.87, E_{opt} = 1.14 eV], [(Co,Cr); R = −0.54, E_{opt} = 1.63 eV], [(Mn,Co); R = −0.43, E_{opt} = 1.38 eV], and [(Fe,V); R = −0.41, E_{opt} = 1.76 eV] finally survived and will potentially serve as the next record-breaking materials in FPVs.

Importantly, note that, as the suggested materials have yet to be synthesized, we have investigated the thermodynamic stability of the compounds for any future synthetic works. Fig. 5*C* provides the formation energy (E_f) of each compound, $Bi_2(B',B'')O_6$, with respect to the decomposition into $BiB'O_3$ and $BiB''O_3$. Many of the candidate materials of R < 0 have negative formation energies (*SI Appendix*, Table S7), which inspiringly indicates that they have the potential to be experimentally synthesized.

Conclusions

Double-perovskite BFCO is undoubtedly the best performing active-layer material for FPVs and has indeed made FPVs much more competitive with conventional devices. The excellent performance was previously attributed primarily to the reduced band gap and resultant increase in solar absorption; however, our quantitative analysis reveals that this factor is not the primary reason. Based on electronic structure calculations of BFCO, we clarify that the photoexcited electron and hole states are spatially separated onto the Fe and Cr sites, respectively. Such *e-h* separation becomes much more pronounced in disordered phases, which is critical to understanding the extremely high photocurrents in BFCO-based FPV devices. In addition to providing an understanding of BFCO materials, the present work further suggests the next-generation FPV materials that can potentially outperform BFCO. As a result of exploring 44 additional Bi-based double-perovskite

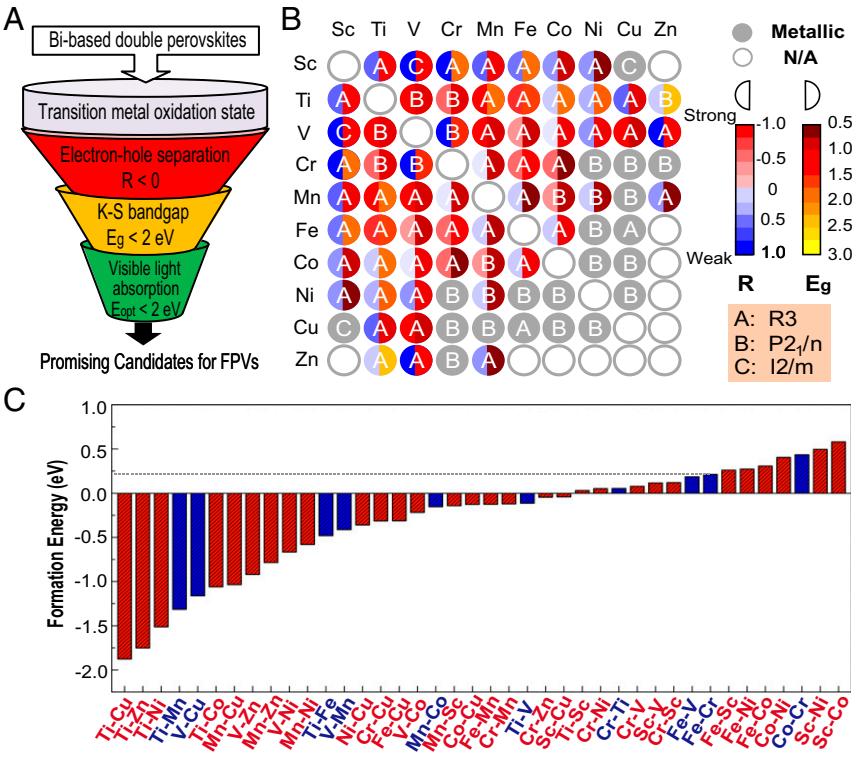

Fig. 5. In search of candidate materials with efficient FPV responses. (*A*) A schematic describing the screening process to search for promising double-perovskite materials in FPVs. The 45 tested materials are all $Bi_2(B',B'')O_6$-type double-perovskite structured oxides, where (B′,B″) is a possible combination of transition-metal B-site cations. Materials of the oxidation-state mismatch are prescreened. For the fast screening, we reasonably assumed G AFM and ordered geometries. (*B*) The degree of *e-h* separation (left semicircle) and band gap (right semicircle) of these oxides are shown with the color mapping. Digits are available in *SI Appendix*, Tables S5 and S6. The alphabet (A, B, C) inside each circle represents the ground-state phase. In reality, the open gray circle cases cannot exist due to oxidation-state mismatch. The closed gray circles represent metallic samples. (*C*) Formation energies (E_f) of the $Bi_2(B',B'')O_6$ compounds with respect to the decomposition into $BiB'O_3$ and $BiB''O_3$. Ten (B′,B″) combinations showing negative R values are highlighted in blue. Most compounds have lower formation energies relative to that of the BFCO material (represented by the dashed line).

oxides, we propose five materials that offer a combination of strong *e-h* separations and visible-light absorptions for FPV applications.

Methods

First-Principles Calculations. DFT calculations were performed using the plane-wave-basis Vienna ab initio simulation package (VASP) code (33, 34) with an energy cutoff of 500 eV. The projector augmented-wave method was adopted to describe the potential of the ionic cores. We employed the generalized gradient approximation plus the Hubbard U method (35) with the Perdew–Burke–Ernzerhof exchange-correlation functional (36). For all BFCO oxides in the present work, we adopted $U = 4$ eV and $J = 0.8$ eV for both Fe and Cr 3*d* orbitals, as described in previous reports, to accurately describe the band structures of BFCO (19, 20). For the additional 44 double-perovskite oxides [$Bi_2(B'B'')O_6$] in Fig. 5, we applied the same Hubbard U parameters, $U = 4$ eV and $J = 0.8$ eV, to the valence *d* orbitals of both B′ and B″ ions. We used different ***k***-point meshes, depending on the cell sizes. For the simulation cells in Figs. 1, 2, 4, and 5, Brillouin-zone integrations were performed using Monkhorst–Pack ***k***-point samplings of $3 \times 3 \times 3$ for structural relaxation, and $9 \times 9 \times 9$ for band structures and charge densities. For the $8 \times 8 \times 2$ supercell shown in Fig. 3*A* ***k***-point mesh of $1 \times 1 \times 4$ was chosen for both geometry relaxation and charge density calculations. The geometry was fully relaxed until the maximum Hellmann–Feynman forces are less than 0.01 eV·Å^{-1}. Lattice parameters of all simulated BFCO structures are shown in *SI Appendix*, Table S8, and our predictions are excellent, with a *c*/*a* ratio of less than 1.6% for all cases. For the newly designed materials, both cell parameters and atom coordinates are relaxed, and the relaxed lattice parameters are shown in *SI Appendix*, Table S9. E_g values predicted using the DFT+U scheme for new materials may differ from their experimental counterparts; comparisons are not possible at the present stage, due to the absence of experimental data. Electronic structure results of hybrid density functional (HSE06) of a select BFCO structure are available in *SI Appendix*, Fig. S11.

Absorption Spectra Calculations. Absorption spectra were obtained by computing the complex frequency-dependent dielectric matrix via sums over allowed transitions in random-phase approximation schemes (37). The absorption coefficients [$\alpha(\omega)$] were calculated from the following equation:

$$\alpha(\omega) = \frac{2\omega}{c}\left(\frac{\sqrt{\varepsilon_1^2(\omega)+\varepsilon_2^2(\omega)}-\varepsilon_1(\omega)}{2}\right)^{1/2},$$

where ε_1 and ε_2 are the real and imaginary parts, respectively, of the dielectric function, ω is the photon frequency, and c is the speed of light. The optical threshold energy (E_{opt}) is quantitatively defined as the lowest photon energy at which the absorption amount reaches 50%. From Beer–Lambert's law [i.e., absorption (%) $= 1 - \exp(-\boldsymbol{\alpha}\cdot\mathbf{d})$], $\boldsymbol{\alpha}$ that makes 50% absorption is 0.69×10^5 cm^{-1} at **d** of 100 nm (typical experimental thickness).

Effective Mass Calculations. The effective mass (m^*) was calculated according to

$$m^* = \pm\hbar^2\left(\frac{d^2E}{dk^2}\right)^{-1},$$

where $\hbar$ is the reduced Planck constant and E is the energy of a band as a function of the wave vector ***k***. The fitting range is $|\boldsymbol{k}| < 0.05$ Å^{-1}.

Quantification of the Degree of *e-h* Separation. The degree of *e-h* separation was estimated by introducing a DOS-related factor (R), which is defined as

$$R = \left(\frac{S_{B'}-S_{B''}}{S_{B'}+S_{B''}}\right)_{CBM} \times \left(\frac{S_{B'}-S_{B''}}{S_{B'}+S_{B''}}\right)_{VBM},$$

where $S_{B'}$ and $S_{B''}$ are the integrated DOS values of the B′ and B″ cation, respectively, in the immediate vicinity of either CBM or VBM. The integration was performed over an energy range of 0.05 eV (see *SI Appendix*, Fig. S12 for the related schematic diagram). Systems with the more negative R values offer stronger spatial charge separations.

ACKNOWLEDGMENTS. This work was supported by the National Research Foundation (Grant 2016R 1D1A1B 03933253) of Korea, and an institutional project of Korea Institute of Science and Technology (Project 2E28000).

1. Shockley W, Queisser HJ (1961) Detailed balance limit of efficiency of *p-n* junction solar cells. *J Appl Phys* 32:510–519.
2. Yang SY, et al. (2010) Above-bandgap voltages from ferroelectric photovoltaic devices. *Nat Nanotechnol* 5:143–147.
3. Choi T, Lee S, Choi YJ, Kiryukhin V, Cheong SW (2009) Switchable ferroelectric diode and photovoltaic effect in $BiFeO_3$. *Science* 324:63–66.
4. Alexe M, Hesse D (2011) Tip-enhanced photovoltaic effects in bismuth ferrite. *Nat Commun* 2:256.
5. Grinberg I, et al. (2013) Perovskite oxides for visible-light-absorbing ferroelectric and photovoltaic materials. *Nature* 503:509–512.
6. Yuan Y, Xiao Z, Yang B, Huang J (2014) Arising applications of ferroelectric materials in photovoltaic devices. *J Mater Chem A* 2:6027–6041.
7. Spanier JE, et al. (2016) Power conversion efficiency exceeding the Shockley-Queisser limit in a ferroelectric insulator. *Nat Photonics* 10:611–616.
8. Yi HT, Choi T, Choi SG, Oh YS, Cheong SW (2011) Mechanism of the switchable photovoltaic effect in ferroelectric $BiFeO_3$. *Adv Mater* 23:3403–3407.
9. Han H, et al. (2015) Switchable photovoltaic effects in hexagonal manganite thin films having narrow band gaps. *Chem Mater* 27:7425–7432.
10. Paillard C, et al. (2016) Photovoltaics with ferroelectrics: Current status and beyond. *Adv Mater* 28:5153–5168.
11. Zhang J, et al. (2013) Enlarging photovoltaic effect: Combination of classic photoelectric and ferroelectric photovoltaic effects. *Sci Rep* 3:2109.
12. Choi WS, et al. (2012) Wide bandgap tunability in complex transition metal oxides by site-specific substitution. *Nat Commun* 3:689.
13. Gou G, Charles N, Shi J, Rondinelli JM (2017) A-site ordered double perovskite $CaMnTi_2O_6$ as a multifunctional piezoelectric and ferroelectric-photovoltaic material. *Inorg Chem* 56:11854–11861.
14. Song S, et al. (2017) β-$CuGaO_2$ as a strong candidate material for efficient ferroelectric photovoltaics. *Chem Mater* 29:7596–7603.
15. Bhatnagar A, Chaudhuri AR, Kim YH, Hesse D, Alexe M (2013) Role of domain walls in the abnormal photovoltaic effect in $BiFeO_3$. *Nat Commun* 4:2835.
16. Cao D, et al. (2012) High-efficiency ferroelectric-film solar cells with an n-type Cu_2O cathode buffer layer. *Nano Lett* 12:2803–2809.
17. Chatterjee S, Bera A, Pal AJ (2014) p-i-n heterojunctions with $BiFeO_3$ perovskite nanoparticles and p- and n-type oxides: Photovoltaic properties. *ACS Appl Mater Interfaces* 6:20479–20486.
18. Nechache R, et al. (2015) Bandgap tuning of multiferroic oxide solar cells. *Nat Photonics* 9:61–67.
19. Baettig P, Spaldin NA (2005) Ab initio prediction of a multiferroic with large polarization and magnetization. *Appl Phys Lett* 86:012505.
20. Baettig P, Ederer C, Spaldin NA (2005) First principles study of the multiferroics $BiFeO_3$, Bi_2FeCrO_6, and $BiCrO_3$: Structure, polarization, and magnetic ordering temperature. *Phys Rev B Condens Matter Mater Phys* 72:214105.
21. Nechache R, et al. (2009) Epitaxial thin films of the multiferroic double perovskite Bi_2FeCrO_6 grown on (001)-oriented $SrTiO_3$ substrates: Growth, characterization, and optimization. *J Appl Phys* 105:061621.
22. Nechache R, et al. (2011) Epitaxial patterning of Bi_2FeCrO_6 double perovskite nanostructures: Multiferroic at room temperature. *Adv Mater* 23:1724–1729.
23. Nechache R, et al. (2011) Photovoltaic properties of Bi_2FeCrO_6 epitaxial thin films. *Appl Phys Lett* 98:202902.
24. Rout PC, Putatunda A, Srinivasan V (2016) Origin of lowered magnetic moments in epitaxially strained films of multiferroic Bi_2FeCrO_6. *Phys Rev B* 93:104415.
25. Goffinet M, Iniguez J, Ghosez P (2012) First-principles study of a pressure-induced spin transition in multiferroic Bi_2FeCrO_6. *Phys Rev B Condens Matter Mater Phys* 86:024415.
26. Fujii K, et al. (2013) Experimental visualization of the Bi-O covalency in ferroelectric bismuth ferrite ($BiFeO_3$) by synchrotron X-ray powder diffraction analysis. *Phys Chem Chem Phys* 15:6779–6782.
27. Tong WY, Ding HC, Gong SJ, Wan X, Duan CG (2015) Magnetic ordering induced giant optical property change in tetragonal $BiFeO_3$. *Sci Rep* 5:17993.
28. Dexter DL (1958) Theory of the optical properties of imperfections in nonmetals. *Solid State Phys* 6:353–411.
29. Sakurai JJ (1994) *Modern Quantum Mechanics*, ed Tuan SF (Addison-Wesley, Reading, MA), pp 285–345.
30. Goodenough JB (1955) Theory of the role of covalence in the perovskite-type manganites [La,M(II)]MnO_3. *Phys Rev* 100:564.
31. Kanamori J (1959) Superexchange interaction and symmetry properties of electron orbitals. *J Phys Chem Solids* 10:87–98.
32. Lufaso MW, Barnes PW, Woodward PM (2006) Structure prediction of ordered and disordered multiple octahedral cation perovskites using SPuDS. *Acta Crystallogr B* 62:397–410.
33. Kresse G, Furthmüller J (1996) Efficient iterative schemes for *ab initio* total-energy calculations using a plane-wave basis set. *Phys Rev B Condens Matter* 54:11169–11186.
34. Kresse G, Joubert D (1999) From ultrasoft pseudopotentials to the projector augmented-wave method. *Phys Rev B Condens Matter Mater Phys* 59:1758–1775.
35. Cococcioni M, de Gironcoli S (2005) Linear response approach to the calculation of the effective interaction parameters in the LDA+U method. *Phys Rev B Condens Matter Mater Phys* 71:035105.
36. Perdew JP, Burke K, Ernzerhof M (1996) Generalized gradient approximation made simple. *Phys Rev Lett* 77:3865–3868.
37. Bohm D, Pines D (1951) A collective description of electron interactions. I. Magnetic interactions. *Phys Rev* 82:625–634.